Structure of dipole bands in doubly odd ^{102}Ag

V. Singh,[1] S. Sihotra,[1,*] S. S. Malik,[2] G. H. Bhat,[3] R. Palit,[4] J. A. Sheikh,[3] S. Kumar,[1] N. Singh,[1] K. Singh,[1] J. Goswamy,[1] J. Sethi,[4] S. Saha,[4] T. Trivedi,[4] and D. Mehta[1]

[1]*Department of Physics, Panjab University, Chandigarh-160014, India*
[2]*Department of Physics, GNDU, Amritsar-143005, India*
[3]*Department of Physics, University of Kashmir, Srinagar-190006, India*
[4]*Department of Nuclear and Atomic Physics, TIFR, Mumbai-400005, India*

(Received 25 July 2016; published 21 October 2016)

Excited states in the transitional doubly odd ^{102}Ag nucleus were populated in the ^{75}As(^{31}P, $p3n$) fusion-evaporation reaction using the 125 MeV incident ^{31}P beam. The subsequent deexcitations were investigated through in-beam γ-ray spectroscopic techniques using the Indian National Gamma Array spectrometer equipped with 21 clover Ge detectors. The level scheme in ^{102}Ag has been established up to excitation energy ~6.5 MeV and angular momentum 19$\hbar$. The earlier reported level scheme is considerably extended and modified to result in a pair of nearly degenerate negative-parity dipole bands. Lifetime measurements for the states of these two dipole bands have been performed by using the Doppler-shift attenuation method. The two nearly degenerate bands exhibit different features with regard to kinetic moment of inertia, and the reduced transition probabilities B($M1$) and B($E2$), which do not favor these to be chiral partners. These bands are discussed in the framework of the hybrid version of tilted-axis cranking (TAC) model calculations and assigned the $\pi g_{9/2} \otimes \nu h_{11/2}$ and $\pi g_{9/2} \otimes \nu h_{11/2}(d_{5/2}/g_{7/2})^2$ configurations. The TAC model calculations are extended to the nearly degenerate bands observed in the heavier doubly odd $^{104-108}$Ag isotopes.

DOI: 10.1103/PhysRevC.94.044320

I. INTRODUCTION

For the spherical transitional nuclei in mass $A \sim 100$–110 region close to the $N = Z = 50$ shell closure, the valence proton space consists of the $g_{9/2}$, $p_{1/2}$, $f_{5/2}$, and $p_{3/2}$ orbitals, and the valence neutron space consists of the $h_{11/2}$, $s_{1/2}$, $g_{7/2}$, and $d_{5/2}$ orbitals. Deformation is generated by the particle-hole excitations across the proton major shell gaps. The anisotropic current distribution of particles and holes in the high-j orbitals such as $\nu h_{11/2}$ and $\pi g_{9/2}$, respectively, are expected to result into bands with angular-momentum generation based on the shears mechanism. One shears-like (magnetic rotation) [1] and two shears-like (antimagnetic rotation) [2,3] manifestations of the shears mechanism have successfully explained the observed characteristic features of the band structures in the mass $A \sim 100$ region. Furthermore, delicate interplay of the strongly oblate-shape ($\gamma = -60^\circ$) driving high-Ω $\pi g_{9/2}$ and prolate-shape ($\gamma = 0^\circ$) driving low-Ω $\nu h_{11/2}$ orbitals in the configurations results in triaxial (γ-soft) shapes with modest deformation ($\beta_2 \sim 0.1$) [4,5]. One important piece of spectroscopic evidence indirectly indicating triaxial nuclear shape is the spin chirality [6]. It results from restoration of spontaneous chiral symmetry breaking in a triaxial nucleus in the laboratory frame and leads to a pair of nearly degenerate rotational bands with the same parity. In addition, these bands are supposed to exhibit nearly similar features with regard to moment of inertia (MOI), quasiparticle alignment, signature staggering behavior, and, more importantly, the transition probabilities. Some fingerprints of nuclear chirality have been identified in the mass $A \sim 100$ region, where nearly degenerate doublet bands have been observed in the doubly odd ^{98,100}Tc$_{43}$ [7,8], $^{100-106}$Rh$_{45}$ [9–12], and $^{104-108}$Ag$_{47}$ [13–18] nuclei. However, the risk of misinterpreting these bands as chiral partners [19] necessitates stringent tests because most of these band pairs are found to differ in one or more descriptions; viz., MOI, transition probabilities, etc. Considerable experimental and theoretical efforts are underway to understand such conundrums and bands have been interpreted in terms of two different prospects; namely, distinct quasiparticle structures or distinct shapes. Recently in ^{106}Ag, Leider *et al.* [20] concluded from the γ-spectroscopic studies including precise lifetime measurements and the particle-rotor-model calculations that the observed nearly degenerate bands do not form a pair of chiral partner bands; rather, these originate due to the two different quasiparticle structures; namely, $\pi g_{9/2} \otimes \nu h_{11/2}$ and $\pi g_{9/2} \otimes \nu h_{11/2}(d_{5/2}/g_{7/2})^2$. The band structures have also been explained on the basis of microscopic triaxial projected shell-model calculations [21] as based on same quasiparticle $\pi g_{9/2} \otimes \nu h_{11/2}$ configurations with the $K = 4$ band diabatically crossed by the $K = 2$ band at spin 14$\hbar$.

In the present work, the nuclear structure investigations have been carried out in the doubly odd ^{102}Ag nucleus through γ-ray spectroscopic techniques including the lifetime measurements based on the Doppler-shift attenuation method (DSAM) using powerful clover detector array. Nearly degenerate dipole bands have already been observed in the neighboring $N = 55$ isotones, ^{98}Tc [7], and ^{100}Rh [9]. The observed level structures in ^{102}Ag are assigned Nilsson configurations on the basis of observed quasiparticle pair alignments, band-crossing frequencies, and experimentally deduced B($M1$) and B($E2$) transition probabilities, and discussed within the framework of the hybrid version of tilted-axis cranking (TAC) model calculations [22,23].

*ssihotra@pu.ac.in

 ©2016 American Physical Society

II. EXPERIMENTAL DETAILS AND DATA ANALYSIS

Excited states in the ^{102}Ag nucleus were populated in the ^{75}As(^{31}P, $p3n$)^{102}Ag fusion-evaporation reaction at $E_{\rm lab} = 125$ MeV. The ^{31}P beam was provided by the Pelletron-LINAC facility at TIFR, Mumbai. The ^{75}As target of thickness 2.8 mg/cm^2 was prepared by vacuum evaporation and rolled onto a 10 mg/cm^2 thick Pb backing. The recoiling nuclei had a maximum initial velocity of $v/c = 2.7\%$ in the target. The deexciting γ rays were detected by using the Indian National Gamma Array (INGA) consisting of 21 Compton-suppressed clover detectors [24,25]. The minimum threshold of the INGA set up is around 50 keV. Twofold and higher clover coincidence events were recorded in a fast digital data acquisition system based on Pixie-16 modules of XIA LLC [25]. The efficiency of the array was obtained by fitting a seven-parameter function (EFFIT) using the RADWARE package [26]. The efficiency of the array was measured for energies from 52 to 1408 keV using a mixed ^{152}Eu-^{133}Ba standard radioactive source and up to ~2.5 MeV from the intensity balance in the γ deexcitations of ^{38}Ar, ^{39}K, ^{93}Tc, and ^{96}Ru nuclides produced in the present experiment [27].

The data-sorting routine "multiparameter time-stamped-based coincidence search program" (MARCOS), developed at TIFR, sorts the time-stamped data to generate $E_\gamma - E_\gamma$ matrices and $E_\gamma - E_\gamma - E_\gamma$ cubes compatible with the RADWARE format [26]. There were 3.2×10^8 events in the cube which were analyzed by using the RADWARE program LEVIT8R [26] to develop the level scheme. Improved sensitivity was achievable because of a larger fraction of the higher-fold γ-ray coincidence events collected by using INGA and because of the use of clover detectors in the addback mode. The selectivity afforded by "double gating" and the presence of many crossover transitions in the level scheme of ^{102}Ag provide many checks on the placement and ordering of transitions and serve to augment confidence in the correctness of the proposed level scheme. Relative intensities of γ rays in the populated ^{102}Ag nucleus have been extracted from the singles spectra and the γ-γ coincidence spectra. Table I lists all γ rays assigned to the level scheme of ^{102}Ag along with their intensities and the suggested placements in the level scheme shown in Fig. 1.

The spin-parity assignments of the excited nuclear states have been deduced mainly from the directional correlations of oriented states (DCO) [28,29] and the integrated polarization directional correlation from oriented nuclei (IPDCO) analysis [30]. The DCO ratio analysis has been used to identify the dipole and quadrupole transitions by setting gates on the known low-lying stretched electric-quadrupole ($E2$) transitions. For the INGA geometry, the expected value of the DCO ratio is typically $\geqslant 1.0$ for the quadrupole transition and $\leqslant 0.6$ for the dipole transition with gate on the stretched $E2$ transition. The DCO ratios of ~1 are, however, also expected for pure $\Delta I = 0$ dipole transitions [29]. The IPDCO analysis has been performed by using two asymmetric polarization matrices corresponding to the parallel and perpendicular segments (with respect to the emission plane) of the clover detector chosen as a Compton polarimeter along one axis and the coincident γ rays in all the detectors along the other axis. A positive value of the IPDCO ratio indicates an electric transition while a negative value indicates a magnetic transition. The DCO and IPDCO ratios along with the assigned multipolarities for various γ transitions are also included in Table I.

The detection of γ rays emitted from the recoiling nuclei slowing down in the thick target with backing exhibited Doppler-broadening effects when observed by detectors at forward, backward, and 90° angles. Lifetimes for the states of negative-parity bands (Fig. 1) were deduced by using the DSAM technique [31]. The lineshapes of γ rays were extracted from the background-subtracted spectra projected from the angle-dependent E_γ-E_γ matrices consisting of events in the forward (23°, 40°) and backward (140°, 157°) detectors along one axis and all other detectors along the second axis. Simultaneous fits were performed for the experimental lineshapes of γ transitions at the forward and backward angles, with the theoretical lineshapes derived from the LINESHAPE program [31]. Shell-corrected Northcliffe and Schilling stopping powers [32] were used for energy-loss calculations. The value of time step and the number of recoil histories were 0.01 ps and 5000, respectively. The best fit was obtained through the least-square-minimization procedures SEEK, SIMPLEX, and MIGRAD [31]. The side feeding into each level of band was considered as a cascade of five transitions having a fixed moment of inertia comparable to that of the in-band sequences. The energies of γ rays and side-feeding intensities were used as input parameters for the lineshape analysis. The χ^2 minimization was obtained by using the subroutine MINUIT [33].

III. RESULTS

A. Level scheme

The level scheme of ^{102}Ag (Fig. 1) based on the ground state $I^\pi = 5^+$ [34] is established up to the excitation energy ~6.5 MeV and spin $19\hbar$. The present level scheme consists of positive-parity bands B1, B2, and B5, and negative-parity bands B3 and B4 (Fig. 1). It preserves basic features of bands B1, B2, and B3 observed previously by Rastikerdar [35], Kumar *et al.* [36], and Treherne *et al.* [37]. Note that the ground-state spin is wrongly shown to be 3^+ in Fig. 4 of Rastikerdar [35] and in Fig. 1 of Kumar *et al.* [36]. The level scheme from earlier investigations [35–37] is modified and extended significantly with the addition of more than 80 new γ transitions (Fig. 1). Various spectra are shown in Figs. 2(a)–2(e).

The positive-parity bands B1 and B2 are based on the 7^+ states at 181- and 382 keV, respectively (Fig. 1). New transitions of 201- and 241 keV from the 7^+ bandhead state of band B2 [Fig. 2(a)], and the 181 keV crossover transition from the 7^+ bandhead state of band B1 to the 5^+ ground state are observed. An unobserved 46 keV transition is proposed from the 187 keV 5^+ state to 6^+ state on the basis of observed coincidence of the 149- and 540 keV transitions with the 141 keV ($6^+ \rightarrow 5^+$) transition [Fig. 2(a)]. A 156 keV level proposed by Treherne *et al.* [34,37] is confirmed on the basis of the 59 and 156 keV transitions observed in coincidence with the higher-lying transitions in band B2 [Fig. 2(a)]. A new 195 keV transition from the 336 keV 6^+ state is placed in the level scheme.

TABLE I. The γ-ray energies E_γ, deexciting-level energies E_i, relative intensities I_γ, and DCO and IPDCO ratios for transitions in ^{102}Ag. The DCO ratios are obtained from the gated spectra on the stretched $E2$ transitions, as mentioned in the text. The uncertainty in energies of intense γ rays is 0.3 keV. It increases up to 1.0 keV for the weak high-energy γ rays.

E_γ (keV)	E_i (keV)	Intensity	Spin assignment $(I_i^\pi \to I_f^\pi)$	DCO	IPDCO	Multipolarity assignment
31	187		$5^+ \to 3^+$			
40	181		$7^+ \to 6^+$			
46	187		$5^+ \to 6^+$			
46	382		$7^+ \to 6^+$			
59.1	156	25 (4)	$3^+ \to 4^+$			
89.6	187	106 (7)	$5^+ \to 4^+$			$M1$
97.1	97	108 (8)	$4^+ \to 5^+$			$M1$
98.3	1020	6 (1)	$9^+ \to 8^+$			$M1$
111.1	2847	16 (2)	$13^+ \to 12^+$			$M1$
130.3	1896	24 (4)	$11^+ \to 10^+$	0.56 (9)		$M1$
134.4	3177	17 (2)	$12^- \to 12^+$			
140.7	5943	30 (6)	$\to 18^-$			
141.0	141	1000 (50)	$6^+ \to 5^+$			$M1$
149.0	336	183 (14)	$6^+ \to 5+$			$M1$
156.2	156	28 (4)	$3^+ \to 5^+$			
157.2	1706	335 (18)	$9^- \to 8^-$	0.53 (4)		$M1$
174.1	1020	72 (6)	$9^+ \to 8^+$	0.63 (8)		$M1$
181.0	181	89 (8)	$7^+ \to 5^+$			$E2$
181.5	1202	8 (2)	$9^+ \to 9^+$			
187.1	187	155 (11)	$5^+ \to 5^+$			
189.7	4872	~2	$\to 16^-$			
194.8	336	21 (3)	$6^+ \to 6^+$			
195.5	3043	60 (5)	$12^+ \to 13^+$	0.63 (8)		$M1$
195.8[a]	2300	5 (1)	$\to 10^-$			
200.8	382	19 (3)	$7^+ \to 7^+$			
204.7	3558	7 (2)	$(13^+) \to (12^+)$			$(M1)$
209.7	5375	6 (1)	$\to 17^-$			
237.0	3177	115 (8)	$12^- \to 11^-$	0.63 (5)	−0.13 (3)	$M1$
241.3	382	25 (3)	$7^+ \to 6^+$	0.48 (9)		$M1$
250.6	2454	16 (2)	$11^- \to 10^+$	0.69 (12)		$E1$
256.0	3177	7 (1)	$12^- \to 12^-$			
260.8	3713	206 (14)	$14^- \to 13^-$	0.64 (5)	−0.09 (2)	$M1$
261.2[a]	3771	3 (1)				
266.8	2940	36 (5)	$11^- \to 10^-$	0.50 (8)	−0.17 (4)	$M1$
274.8	3196	229 (16)	$13^- \to 12^-$	0.60 (5)	−0.14 (3)	$M1$
275.1	3452	180 (12)	$13^- \to 12^-$	0.58 (4)	−0.08 (2)	$M1$
279.8	1202	51 (5)	$9^+ \to 8^+$	0.66 (9)	−0.04 (1)	$M1$
304.0	3713	129 (8)	$14^- \to 13^-$	0.52 (4)	−0.14 (1)	$M1$
306.6	3043	12 (2)	$12^+ \to 12^+$			
318.6[a]	2025	10 (2)	$\to 9^-$			
336.2	336	185 (13)	$6^+ \to 5^+$			$M1$
349.8	2454	353 (18)	$11^- \to 10^-$	0.49 (4)	−0.16 (1)	$M1$
380.8[a]	2277	12 (2)	$\to 11^+$			
397.8	2104	413 (21)	$10^- \to 9^-$	0.53 (4)	−0.06 (2)	$M1$
408.7	6366	10 (2)	$(18^+) \to 17^+$			$(M1)$
412.9	2616	21 (3)	$(11^+) \to 10^+$	0.54 (10)		$(M1)$
423.1	5957	10 (2)	$17^+ \to (16^+)$	0.54 (11)		$(M1)$
428.4[a]	2882	29 (4)	$\to 11^-$			
464.1	846	65 (6)	$8^+ \to 7^+$	0.46 (7)	−0.09 (4)	$M1$
466.1	4179	146 (12)	$15^- \to 14^-$	0.44 (5)	−0.06 (1)	$M1$
467.3	2921	397 (24)	$12^- \to 11^-$			$M1$
479.8	5162	58 (5)	$(16^-) \to 16^-$			
482.0[a]	3952	~1				
483.0[a]	3918	14 (3)				

TABLE I. (*Continued.*)

E_γ (keV)	E_i (keV)	Intensity	Spin assignment $(I_i^\pi \rightarrow I_f^\pi)$	DCO	IPDCO	Multipolarity assignment
483.2	5165	89 (8)	$17^- \rightarrow 16^-$	0.35 (5)	−0.06 (1)	$M1$
486.2	2940	11 (2)	$11^- \rightarrow 11^-$			
487.7	3409	180 (14)	$13^- \rightarrow 12^-$	0.45 (4)	−0.16 (2)	$M1$
488.1[a]	4406	9 (2)				
502.7[a]	4019	∼2				
502.9	4682	119 (10)	$16^- \rightarrow 15^-$	0.35 (4)	−0.06 (1)	$M1$
503.9	3177	8 (2)	$12^- \rightarrow 10^-$			$E2$
510.1	2349	26 (3)	$11^+ \rightarrow 10^+$			$M1$
512.2	3452	20 (4)	$13^- \rightarrow 11^-$			$E2$
517.3	3713	154 (11)	$14^- \rightarrow 13^-$	0.52 (5)	−0.13 (2)	$M1$
531.2	3452	14 (3)	$13^- \rightarrow 12^-$			$M1$
534.8	5952	∼2	$(17^+) \rightarrow 16^+$			$(M1)$
535.8	3713	33 (5)	$14^- \rightarrow 12^-$	1.03 (16)	0.18 (4)	$E2$
540.0	5286	21 (3)	$16^+ \rightarrow 15^+$	0.47 (9)		$M1$
540.1	922	57 (5)	$8^+ \rightarrow 7^+$	0.66 (8)	−0.09 (2)	$M1$
553.3[a]	3435	19 (3)				
555.1	2940	22 (3)	$11^- \rightarrow 10^+$			$E1$
555.4	2104	11 (2)	$10^- \rightarrow 8^-$	0.96 (20)		$E2$
557.6[a]	3841	16 (3)				
561.1	3177	15 (2)	$12^- \rightarrow (11^+)$	0.55 (8)		$(E1)$
569.3	2673	12 (2)	$10^- \rightarrow 10^-$			
582.5	2349	15 (2)	$11^+ \rightarrow 10^+$	0.50 (9)		$M1$
614.8	2454	8 (2)	$11^- \rightarrow 10^+$			$E1$
617.0	3353	17 (2)	$(12^+) \rightarrow 12^+$			
627.1	1549	44 (4)	$8^- \rightarrow 8^+$	0.89 (9)	0.14 (2)	$E1$
637.1	1839	29 (4)	$10^+ \rightarrow 9^+$	0.52 (6)	−0.15(2)	$M1$
637.2	5802	32 (5)	$18^- \rightarrow 17^-$	0.47 (6)	−0.09 (2)	$M1$
643.3	5805	24 (4)	$(17^-) \rightarrow (16^-)$			$(M1)$
645.1	5417	11 (2)	$16^+ \rightarrow 15^+$	0.42 (9)		$M1$
650.8	4746	27 (4)	$15^+ \rightarrow 14^+$	0.50 (7)	−0.08 (2)	$M1$
654.5	6457	25 (4)	$19^- \rightarrow 18^-$	0.65 (8)	−0.09 (2)	$M1$
662.8[a]	3510	14 (2)	$\rightarrow 13^+$			
663.1[a]	4133	∼1				
663.2[a]	4758	9 (2)	$\rightarrow 14^+$			
665.1	846	314 (16)	$8^+ \rightarrow 7^+$	0.69 (4)	−0.10 (2)	$M1$
671.3	5957	15 (2)	$17^+ \rightarrow 16^+$	0.52 (9)	−0.13 (3)	$M1$
677.1	4772	12 (2)	$15^+ \rightarrow 14^+$	0.62 (9)	−0.09 (3)	$M1$
685.6	1706	57 (5)	$9^- \rightarrow 9^+$	0.87 (8)	0.06 (2)	$E1$
694.4	1896	71 (6)	$11^+ \rightarrow 9^+$	1.02 (12)	0.10 (2)	$E2$
702.9	1549	102 (7)	$8^- \rightarrow 8^+$	0.92 (8)	0.09 (2)	$E1$
705.1	846	35 (4)	$8^+ \rightarrow 6^+$			$E2$
723.1	3177	33 (4)	$12^- \rightarrow 11^-$	0.44 (7)	−0.08 (3)	$M1$
725.2[a]	4505	∼2				
745.7	1766	83 (7)	$10^+ \rightarrow 9^+$	0.55 (6)	−0.16 (3)	$M1$
747.8	2454	82 (7)	$11^- \rightarrow 9^-$	1.00 (10)	0.13 (3)	$E2$
770.2	4179	20 (3)	$15^- \rightarrow 13^-$	0.91 (17)		$E2$
783.8	1706	11 (2)	$9^- \rightarrow 8^+$	0.63 (9)		$E1$
788.2	5534	12 (2)	$(16^+) \rightarrow 15^+$			$(M1)$
792.2	3713	38 (5)	$14^- \rightarrow 12^-$	1.04 (11)		$E2$
816.5	2921	47 (4)	$12^- \rightarrow 10^-$	1.08 (18)		$E2$
819.6	1202	49 (5)	$9^+ \rightarrow 7^+$	0.99 (10)	0.04 (1)	$E2$
828.2	3177	18 (3)	$12^- \rightarrow 11^+$	0.60 (9)	0.08 (2)	$E1$
834.2	2673	54 (5)	$10^- \rightarrow 10^+$	0.92 (10)	0.05 (1)	$E1$
836.2	2940	51 (5)	$11^- \rightarrow 10^-$	0.57 (5)	−0.06 (1)	$M1$
839.4	1020	893 (45)	$9^+ \rightarrow 7^+$	1.04 (15)	0.15 (2)	$E2$
839.9	2736	62 (7)	$12^+ \rightarrow 11^+$	0.53 (5)	−0.05 (1)	$M1$
860.2	1706	113 (8)	$9^- \rightarrow 8^+$	0.45 (4)	0.06 (1)	$E1$

TABLE I. (*Continued.*)

E_γ (keV)	E_i (keV)	Intensity	Spin assignment $(I_i^\pi \to I_f^\pi)$	DCO	IPDCO	Multipolarity assignment
866.0	3713	19 (4)	$14^- \to 13^+$	0.65 (9)		$E1$
876.0	1896	547 (28)	$11^+ \to 9^+$	0.99 (10)	0.09 (2)	$E2$
938.9[a]	2835	25 (3)	$\to 11^+$			
951.0	2847	308 (16)	$13^+ \to 11^+$	1.01 (14)	0.09 (2)	$E2$
954.9	3409	38 (5)	$13^- \to 11^-$	1.00 (10)	0.06 (2)	$E2$
967.2	2673	58 (6)	$10^- \to 9^-$	0.66 (7)	−0.09 (2)	$M1$
969.2	4682	52 (6)	$16^- \to 14^-$	1.02 (10)	0.10 (2)	$E2$
982.9	4179	34 (5)	$15^- \to 13^-$	1.04 (18)	0.04 (1)	$E2$
986.0	5165	25 (4)	$17^- \to 15^-$	0.96 (16)	0.12 (2)	$E2$
993.9[a]	3841	23 (3)	$\to 13^+$			
998.4	3452	16 (3)	$13^- \to 11^-$	0.99 (12)		$E2$
1024.5	2921	13 (3)	$12^- \to 11^+$	0.55 (6)		$E1$
1041.8	4085	14 (2)	$(14^+) \to 12^+$			$(E2)$
1043.9	2940	26 (4)	$11^- \to 11^+$	0.88 (17)	0.15 (2)	$E1$
1052.2	4095	26 (3)	$14^+ \to 12^+$	0.97 (17)	0.17 (2)	$E2$
1073.1	3177	7 (1)	$12^- \to 10^-$			$E2$
1084.0	2104	32 (4)	$10^- \to 9^+$	0.65 (8)	0.02 (1)	$E1$
1123.9	2673	12 (2)	$10^- \to 8^-$			$E2$
1147.2	2349	20 (3)	$11^+ \to 9^+$			$E2$
1147.2	3043	49 (5)	$12^+ \to 11^+$	0.58 (6)	−0.06 (2)	$M1$
1166.9	1549	9 (2)	$8^- \to 7^+$			$E1$
1174.1	2940	12 (2)	$11^- \to 10^+$	0.63 (11)		$E1$
1182.8	2203	38 (5)	$10^+ \to 9^+$	0.47 (5)	−0.14 (3)	$M1$
1191.1	5286	5 (1)	$16^+ \to 14^+$			$E2$
1206.1	5952	9 (2)	$(17^+) \to 15^+$			$(E2)$
1211.3	5957	7 (2)	$17^+ \to 15^+$			$E2$
1233.9	2940	12 (2)	$11^- \to 9^-$	1.07 (20)		$E2$
1238.0	4085	11 (2)	$(14^+) \to 13^+$			$(M1)$
1247.8	4095	71 (8)	$14^+ \to 13^+$	0.52 (6)	−0.18 (3)	$M1$
1280.8	3177	28 (4)	$12^- \to 11^+$	0.62 (9)	0.08 (3)	$E1$
1292.0	6457	8 (1)	$19^- \to 17^-$			$E2$
1313.7[a]	4161	13 (2)	$\to 13^+$			
1321.9	5417	18 (2)	$16^+ \to 14^+$	1.10 (11)	0.09 (3)	$E2$
1324.9[a]	5105	∼2				
1364.8	2385	24 (3)	$10^+ \to 9^+$	0.39 (8)	−0.13 (3)	$M1$
1367.8	1549	265 (16)	$8^- \to 7^+$	0.64 (7)	0.11 (1)	$E1$
1377.1[a]	4212	10 (2)				
1471.3	2673	3 (1)	$10^- \to 9^+$			$E1$
1503.0[a]	3780	4 (1)				
1573.5[a]	3470	∼2	$\to 11^+$			
1619.9[a]	3516	3 (1)	$\to 11^+$			
1639.9[a]	4487	∼2	$\to 13^+$			
1644.8	4381	5 (1)	$\to 12^+$			
1652.9	2673	12 (2)	$10^- \to 9^+$	0.41 (8)	0.10 (3)	$E1$
1662.0	3558	∼2	$(13^+) \to 11^+$			$(E2)$

[a]Corresponds to γ transitions not shown in Fig. 1. For placement see text.

A cascade of 840-111 keV dipole transitions is placed in parallel with the 951 keV ($13^+ \to 11^+$) $E2$ transition [Fig. 2(b)] and a crossover 705 keV transition ($8^+ \to 6^+$) is placed in band B1. The 9^+ and 11^+ states in band B1 decay via the new 98- and 694 keV transitions to the 8^+ and 9^+ states, respectively, in band B2. Band B2 is extended to the 11^+ state with the addition of 510 and 1147 keV crossover γ transitions [Fig. 2(a)]. The 182- and 583 keV transitions are observed from the 9^+ and 11^+ states in band B2 to the respective 9^+ and 10^+ states in band B1. The previously reported 1183-415 keV transition cascade shown as feeding the 9^+ state in band B1 by Treherne *et al.* [37] is found to be part of the decay from the 12^- state in band B4 to the 9^+ state in band B1 [Fig. 2(b)]. The 1314- and 1640 keV transitions, and the 663-261 keV and the 994-558 keV cascades (not shown in Fig. 1) are also observed to feed the 13^+ state in band B1.

The 4095 keV state is assigned $I^\pi = 14^+$ on the basis of the dipole character of the 1248 keV transition deexciting

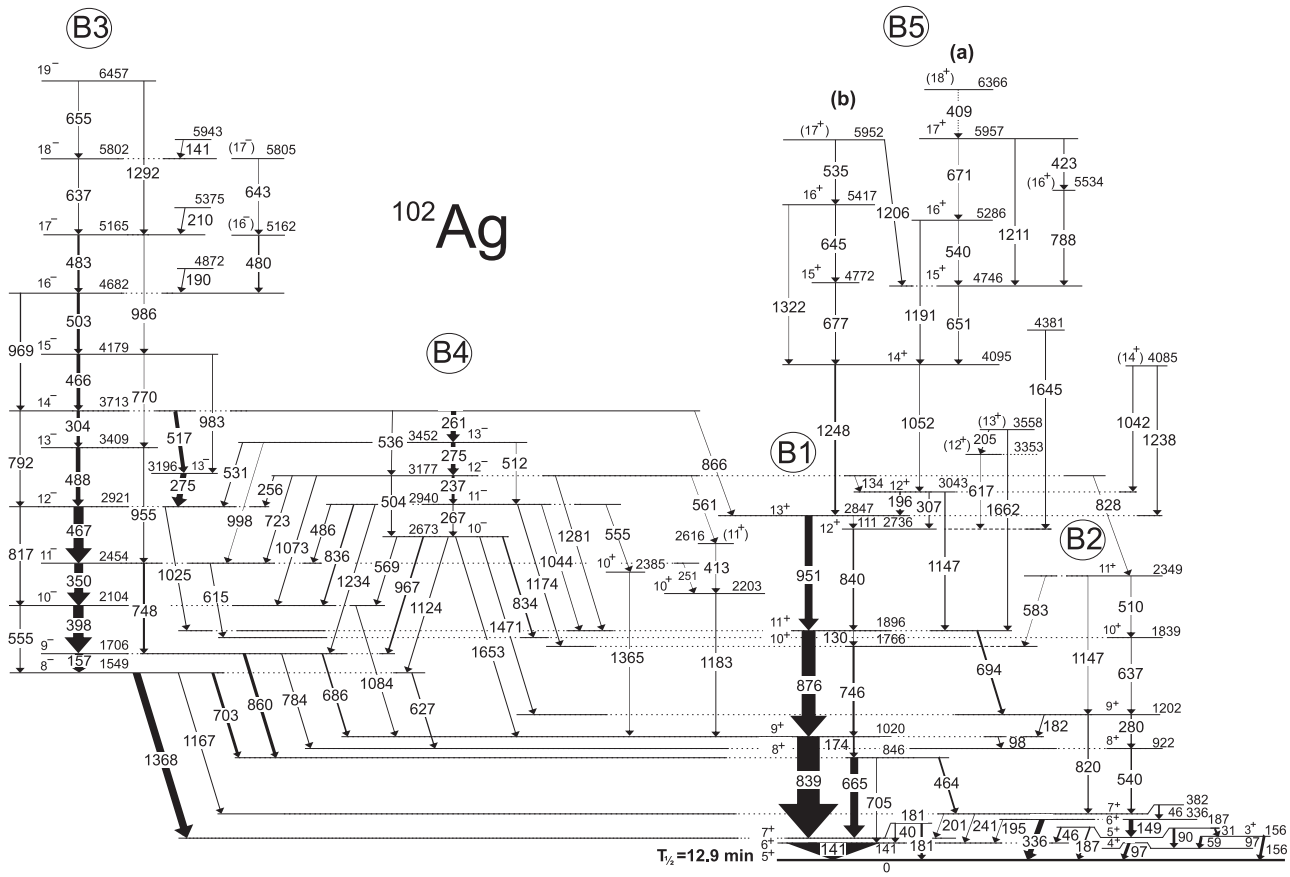

FIG. 1. Level scheme of ^{102}Ag obtained from the present work. Energies of γ rays and levels are given in keV. The width of the arrow representing the γ transition indicates relative intensity of the γ ray.

to the 2847 keV state with $I^{\pi} = 13^{+}$. A new level at 3043 keV is assigned 12^{+} on the basis of (i) its decay to the 11^{+}, 12^{+}, and 13^{+} states via 1147 ($M1$), 307, and 196 keV transitions, respectively, (ii) the quadrupole character of the 1052 keV transition from the 4095 keV state with $I^{\pi} = 14^{+}$, and (iii) the 134 keV transition feeding from the 12^{-} state of band B4. A new (14^{+}) state at 4085 keV is observed which decays to the 12^{+} and 13^{+} states by the 1042- and 1238 keV transitions, respectively [Fig. 2(b)]. The 1620-503, 1574-482(663), 939-1377, and 381-1503-1325(725) keV cascades are observed to feed the 11^{+} state of band B1 in addition to the structure shown in Fig. 1. The level scheme above the 14^{+} state is further extended into the coupled bands labeled B5(a) and B5(b) (Fig. 1), wherein the placement of γ rays is supported by observation of the crossover transitions [Fig. 2(c)].

The present level scheme is considerably different from the ones reported earlier [35–37] with regard to the placement of the γ rays in bands B3 and B4. The sequence of dipole transitions in band B3 is confirmed up to the 19^{-} level through observation of new 770-, 792-, 969-, 986- and 1292 keV crossover transitions [Fig. 2(d) and 2(e)]. Intense parallel cascades of the 488-304 keV and 275-517 keV dipole transitions are observed in the decay of the 14^{-} state. A new crossover 983 keV transition has been observed across the 466- and 517 keV dipole transitions. It is worth mentioning that no crossover transition ($13^{-} \rightarrow 11^{-}$) is observed across the 275- and 467 keV dipole transitions.

In the earlier-reported level schemes [35,36], the 483-, 480-, and 463 keV transitions were placed in a sequence [35,36] above the 16^{-} state. However, in the present work the 480- and 483 keV transitions are not found to be in coincidence and the 463 keV transition. The structure consisting of 637- and 655 keV transitions along with the crossover 1292 keV transition is observed to feed the 16^{-} state through the 483 keV transition (Fig. 1). A cascade of 643-480 keV transitions also feeds the 16^{-} state. The 16^{-}, 17^{-}, and 18^{-} states are fed by new low-energy 190-, 210-, and 141 keV transitions, respectively, and likely form a band.

In the present work, a number of new γ transitions are observed in the decay of band B3 to bands B1 and B2 in addition to the earlier reported 686-, 703-, 860-, 1084-, and 1368 keV interband transitions [35–37] from band B3 to band B1. The 8^{-}, 9^{-}, and 11^{-} states of band B3 decay to the 7^{+}, 8^{+}, and 10^{+} states of band B2 via the 1167-, 784- and 615 keV $E1$ transitions, respectively. Also, the 627 keV transition from the 8^{-} bandhead state of band B3 to the 8^{+} state of band B2 is observed. A new 1025 keV transition from the 12^{-} state of band B3 to the 11^{+} state of band B1 is observed.

A likely cascade of 428-553-483-488 keV possibly dipole transitions (not shown in Fig. 1) is observed to feed the 11^{-} state of band B3. The set of levels observed by Rastikerdar

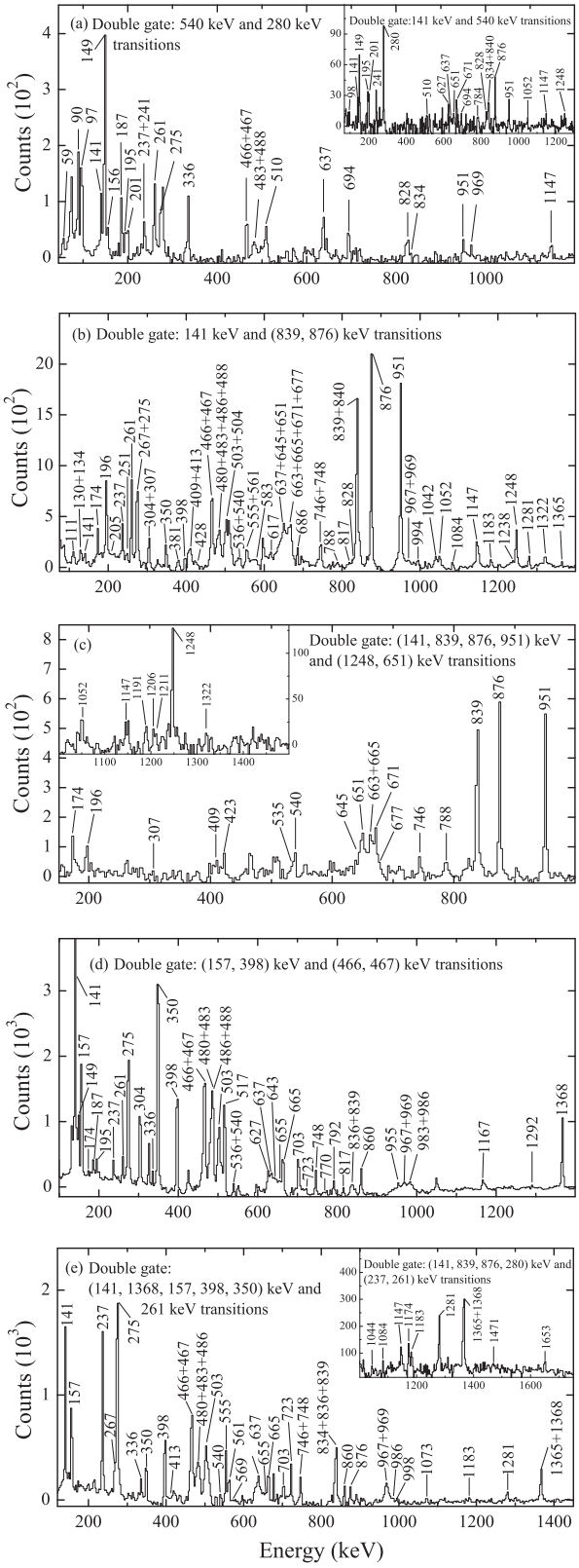

FIG. 2. The double-gated γ-ray coincidence spectra showing the transitions of bands B1–B5 in ^{102}Ag. The spectra are generated with coincidence gate on γ-rays as labeled.

[35] with bandhead at 2179 keV is not confirmed in the present work. Also, the reported decay from the 12^- state to the 9^- state of band B3 via the 2179 keV state [35] is not observed.

The earlier-reported structure consisting of 555-268-275-237-261 keV transition cascade involving a proposed isomeric state at 2117 keV [35,36] with a 13 keV unobserved γ ray decaying to a 10^- state at 2104 keV is considerably modified in the analysis of the present quality data. The transitions have been rearranged into a new band B4 consisting of the 267-237-275-261 keV γ rays and the 555 keV transition is placed in the decay from the 11^- state of band B4 to the 9^+ state of band B1. The placements of transitions in band B4 are confirmed with observation of the 504-, 512-, and 536 keV crossover transitions. The 10^-, 11^-, 12^-, and 13^- states in band B4 decay to the negative-parity states of band B3 through the $\Delta I = 0$, 1, and 2 transitions except that the transition from the 13^- state in band B4 to the 13^- state in band B3 is not observed. The 10^-, 11^-, 12^-, and 14^- states of band B4 decay by the $\Delta I = 1$ transitions to the respective positive-parity states of band B1. The 10^-, 11^-, and 12^- states of band B4 decay to the 9^+ and 10^+ states of band B2, the 11^+ of band B1, and the 11^+ state of band B2, respectively. The lowest observed 2673 keV state in band B4 is assigned $I^\pi = 10^-$ on the basis of (i) the $M1$ character of the 836- and 967 keV transitions (Table I) decaying to the 10^- and 9^- states of band B3, respectively, and (ii) its decay through the 1653 keV ($E1$) and 834 keV ($E1$) transitions to the 9^+ state of band B1 and the 10^+ state of band B2, respectively. Furthermore, the spin-parity to the higher states in band B4 is assigned on the basis of DCO and IPDCO ratios of the 967-, 1174-, and 1281 keV interband transitions and the 267-, 237-, and 275 keV intraband transitions.

B. Lifetime measurements

The lifetime of excited states in bands B3 and B4 were extracted from the lineshape analyses of the Doppler-broadened deexciting γ rays as detected at the forward (23° and 40°), and backward angles (140° and 157°). The 90° spectra were also included in the lineshape analysis to check for contaminant peaks. The lifetime results for the levels of bands B3 and B4 obtained from the present DSAM analysis are given in Table II.

In band B3, the lifetimes could be deduced only for a few states because of presence of close-lying γ rays with energies around 467-, 488-, and 275 keV, and contaminations in various possible gating transitions. The effective lifetime for the $I^\pi = 12^-$ level at 2921 keV in band B3 was deduced to be 1.1 ps

TABLE II. Mean lifetime τ of the levels in bands B3 and B4 in ^{102}Ag. The B($M1$) and B($E2$) are the corresponding reduced transition probabilities. The quoted errors do not include additional systematic errors, which may be as large as 20%.

$I(\hbar)$	Band	τ (ps)	B($M1$)μ_N^2	B($E2$) (eb)^2
10^-	B3	2.93(27)	0.28(3)	0.013(1)
11^-	B3	2.78(25)	0.37(4)	0.022(3)
12^-	B4	1.97(24)	1.00(14)	0.042(6)
13^-	B4	2.21(21)	0.97(10)	0.091(10)

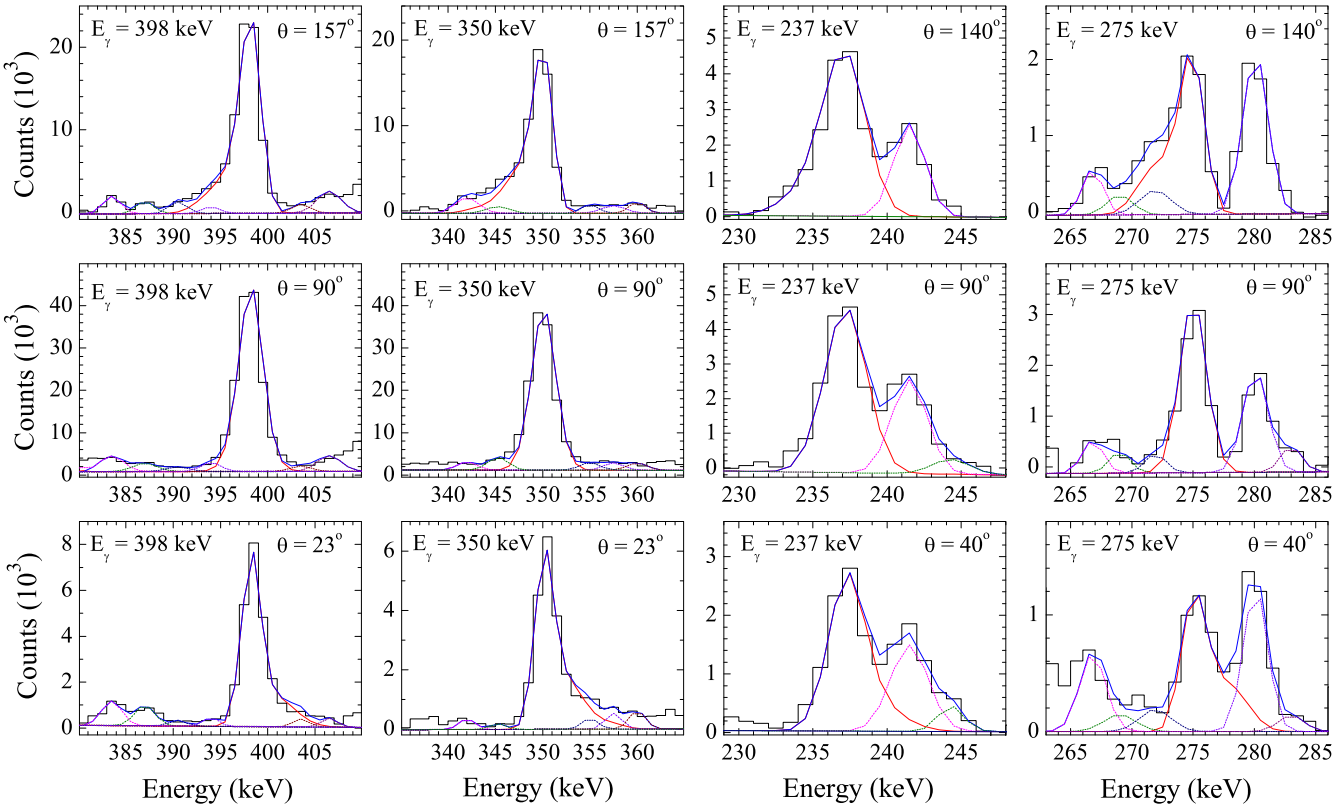

FIG. 3. The lineshape fits for the 398 ($10^- \to 9^-$) keV and 350 ($11^- \to 10^-$) keV transitions in band B3, and the 237 ($12^- \to 11^-$) keV and 275 ($13^- \to 12^-$) keV transitions in band B4, at various angles with respect to the incident beam direction.

by fitting the lineshape of the 817 ($12^- \to 10^-$) keV γ ray in the 141 ($6^+ \to 5^+$) keV γ-ray gated spectra. Due to lack of complete information for the higher-lying levels, the effective lifetime is deduced by assuming 100% side feeding. After fixing the lifetime of the 12^- level, the lifetime of the 11^- and 10^- levels were extracted from lineshape fit of the 350 ($11^- \to 10^-$) and 398 ($10^- \to 9^-$) keV transitions by using the global fitting procedure (Fig. 3). The 141-, 157-, and 1368 keV γ-ray gated spectra were used for this purpose.

The effective lifetime of the $I^\pi = 14^-$ state at 3713 keV was deduced to be 2.5 ps from lineshape fits of (i) the 261 keV γ ray in gated spectra of the 267 keV ($11^- \to 10^-$) γ ray and (ii) the 304 keV γ ray obtained in gated spectra of the 141 keV ($6^+ \to 5^+$) γ ray. The lifetime of the $I^\pi = 12^-$ and 13^- levels in band B4 were extracted from a lineshape fit of the 237- and 275 keV dipole transitions in the 267 keV gated spectra by using the global fitting procedure (Fig. 3).

The uncertainties in the lifetime results were deduced from the χ^2 behavior in the vicinity of the minimum [33] and the side-feeding intensity. It should be noted that the quoted errors do not include additional systematic errors, which may be as large as 20% and stem from the choice of the stopping powers and the effective target thickness used in the analysis. The analysis also involves various assumptions and approximations related to side feeding. The reduced transition probabilities B($M1$) and B($E2$) deduced from the measured lifetimes of the levels in bands B3 and B4 are given in Table II. For the calculations, the $E2/M1$ mixing ratio (δ) = 0 is assumed for the $\Delta I = 1$ transitions.

IV. DISCUSSION

In the doubly odd ^{102}Ag nucleus, the proton fermi surface lies close to the [413]7/2 orbital of the $g_{9/2}$ Nilsson state while the neutron fermi surface lies close to the [420]1/2 orbital of the $g_{7/2}$ state. The $d_{5/2}$ and $g_{7/2}$ states are considerably admixed in their Nilsson configuration. The ground state $I^\pi = 5^+$ is based on the $\pi g_{9/2} \otimes \nu d_{5/2}$ configuration [36,37]. The excitation energy plots for the positive-parity bands B1, B2, and B5, and the negative-parity bands B3 and B4 are given in Figs. 4 and 5(a),

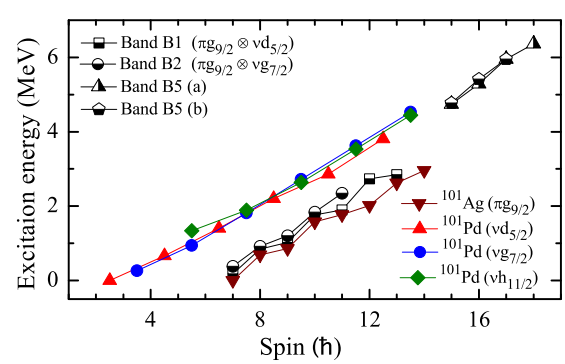

FIG. 4. The excitation energy vs spin plots for bands B1 and B2 in ^{102}Ag, the $\pi g_{9/2}$ band in ^{101}Ag [38], and the $\nu d_{5/2}$, $\nu g_{7/2}$, and $\nu h_{11/2}$ bands in ^{101}Pd [39,40]. The spin values in the $\pi g_{9/2}$ band in ^{101}Ag (with the $9/2^+$ state as bandhead) are shifted by 2.5$\hbar$ for comparison with the $\pi g_{9/2} \otimes \nu d_{5/2}$ and $\pi g_{9/2} \otimes \nu g_{7/2}$ bands (with the 7^+ state as bandhead) in doubly odd ^{102}Ag.

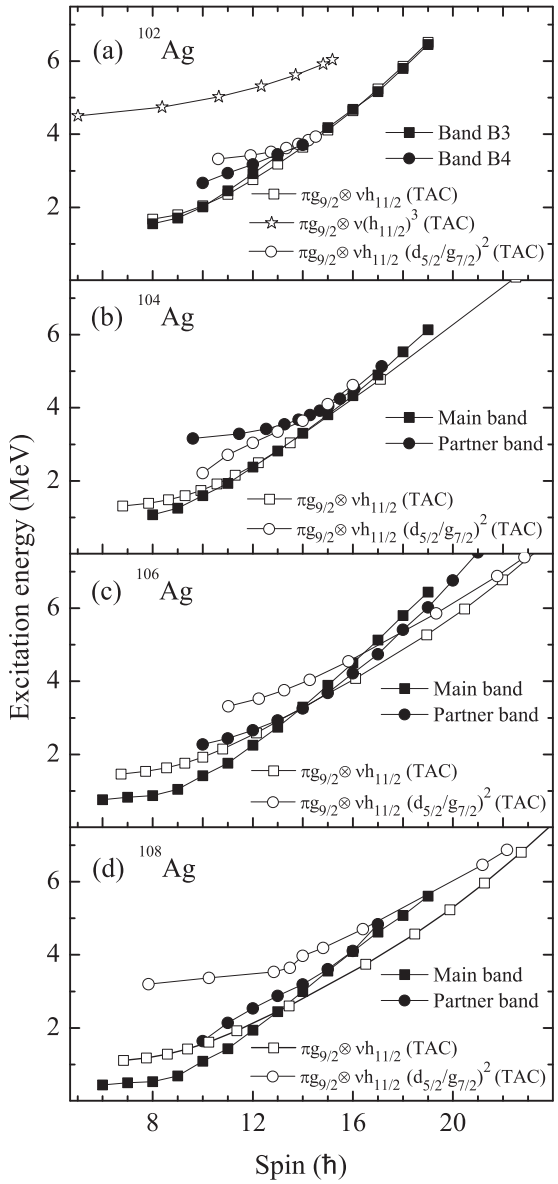

FIG. 5. The comparison of the experimental and TAC-model-calculated excitation energy vs spin plots for the negative-parity doublet bands in doubly odd (a) ^{102}Ag, (b) ^{104}Ag [13], (c) ^{106}Ag [15,16,20], and (d) ^{108}Ag [18] isotopes.

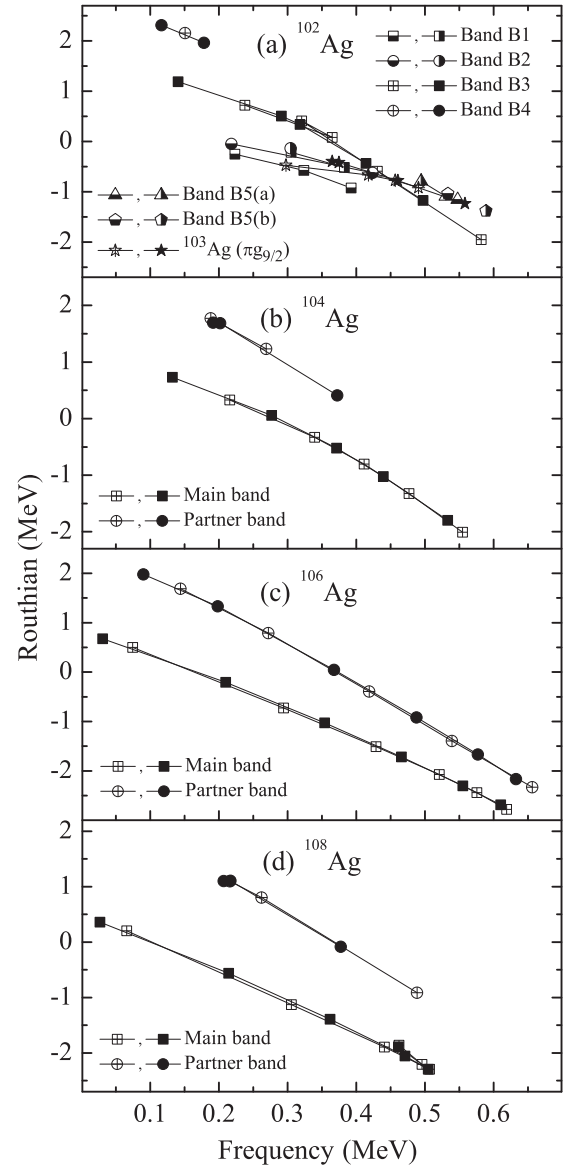

FIG. 6. Experimental Routhian plots for (a) bands B1–B5 in ^{102}Ag and the $\pi g_{9/2}$ band in ^{103}Ag [41], and (b)–(d) negative-parity doublet bands in doubly odd ^{104,106,108}Ag isotopes [13,15,16,18,20].

respectively. For analyzing the rotational properties of the observed bands B1–B5 (Fig. 1), the experimental energies have been transformed into a rotational frame with the prescription of Bengtsson and Frauendorf [42]. The Harris parameters used for subtracting the reference core are $J_0 = 8.9\hbar^2$ MeV^{-1} and $J_1 = 15.7\hbar^4$ MeV^{-3} [43]. The Routhians and alignments for bands B1–B5 in ^{102}Ag are plotted in Figs. 6(a) and 7(a), respectively.

The alignment and the excitation-energy plots for the single quasiparticle $\pi g_{9/2}$ band in the neighboring odd-Z ^{101}Ag [38] and $\nu d_{5/2}$, $\nu g_{7/2}$, and $\nu h_{11/2}$ bands in the neighboring odd-N ^{101}Pd [39,40] nuclei are also given in Figs. 7(b) and 4, respectively, for comparison.

Bands B1 and B2 in ^{102}Ag have been assigned the $\pi g_{9/2} \otimes \nu d_{5/2}$ and $\pi g_{9/2} \otimes \nu g_{7/2}$ Nilsson configurations, respectively [36,37]. The $\pi g_{9/2} \otimes \nu d_{5/2}$ band exhibits signature splitting ~300 keV with the favored signature ($\alpha = 1$) lying lower in energy. The $\pi g_{9/2} \otimes \nu g_{7/2}$ band exhibits signature splitting ~150 keV with the unfavored signature ($\alpha = 1$) lying lower in energy. The Routhian for the favored signature partner in the $\pi g_{9/2} \otimes \nu g_{7/2}$ band (B2) lies ~350 keV above that of the $\pi g_{9/2} \otimes \nu d_{5/2}$ band (B1) [Fig. 6 (a)]. The coupled band B1 has intense $E2$ crossover transitions in the favored ($\alpha = 1$) signature partner and no crossover transitions in the unfavored ($\alpha = 0$) signature partner. In the coupled band B2, the $E2$ crossover transitions are not observed in the favored ($\alpha = 0$) signature partner. The $\pi g_{9/2} \otimes \nu d_{5/2}$ and $\pi g_{9/2} \otimes \nu g_{7/2}$ bands exhibit similar staggering pattern (Fig. 4) and

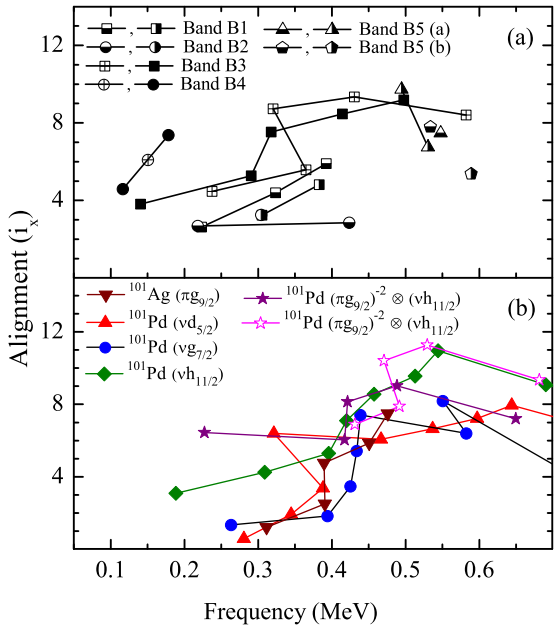

FIG. 7. Experimental alignment plots for (a) bands B1–B5 in ^{102}Ag, and (b) the $\pi g_{9/2}$ band in ^{101}Ag [38], and $\nu d_{5/2}$, $\nu g_{7/2}$, $\nu h_{11/2}$, and $(\pi g_{9/2})^{-2} \otimes \nu h_{11/2}$ bands in ^{101}Pd [39,40].

signature-splitting close to the value ∼200 keV, as observed for the $\pi g_{9/2}$ band in ^{103}Ag [41] [Fig. 6(a)]. This implies that the $\nu d_{5/2}$ and $\nu g_{7/2}$ are likely spectator participants in the respective configurations. The B($M1$)/B($E2$) values for the 9^+, 11^+, and 13^+ states of band B1 are ∼5, 7, and $21\mu_N^2 e^{-2}\mathrm{b}^{-2}$, respectively, and those for the 9^+ and 11^+ states of band B2 are $\sim 12\mu_N^2 e^{-2}\mathrm{b}^{-2}$. These high values also support presence of the $\pi g_{9/2}$ quasiparticle in the configurations. The bands B5(a) and B5(b) exhibit small signature splitting (Fig. 6) and high alignment values (Fig. 7). The B($M1$)/B($E2$) values for the 15^+ and 17^+ states in band B5(a) are ∼40 and $\sim 15\mu_N^2 e^{-2}\mathrm{b}^{-2}$, respectively, and that for the 16^+ state in band B5(b) is $\sim 5\mu_N^2 e^{-2}\mathrm{b}^{-2}$. These positive-parity bands are likely to be based on the $\pi g_{9/2} \otimes \nu(d_{5/2}/g_{7/2}) \otimes \nu(h_{11/2})^2$ configurations.

The negative-parity band B3 in ^{102}Ag is based on the $\pi g_{9/2} \otimes \nu h_{11/2}$ configuration [36,37]. Bands based on this configuration have been systematically observed in the doubly odd $^{104-108}$Ag isotopes [13,15,16,18,20]. The additivity of alignment argument supports the assigned configuration. Band B3 exhibits band crossing at 0.32 MeV with an alignment gain of $\sim 3\hbar$. For the $\pi g_{9/2} \otimes \nu h_{11/2}$ configuration, alignment of the $(\nu h_{11/2})^2$ and $(\pi g_{9/2})^2$ quasiparticle pairs are blocked. The $\nu h_{11/2}$ band in ^{101}Pd exhibits band crossing at $\hbar\omega \sim 0.41$ MeV with alignment gain of $\sim 8\hbar$, which correspond to the $(\pi g_{9/2})^2$ alignment followed by the $(\nu g_{7/2})^2$ alignment [40]. Therefore, the observed small alignment $\sim 3\hbar$ is supportive of the $(\nu g_{7/2})^2$ alignment. The observed band crossing frequency in band B3 in ^{102}Ag is relatively lower than expected. It is worth mentioning that the signature splitting for the $\pi g_{9/2} \otimes \nu h_{11/2}$ band in ^{102}Ag is quenched to $\Delta e' \sim 30$ keV, as compared to ∼200 keV as observed for the $\pi g_{9/2}$ bands in ^{101,103}Ag [38,41]. The signature splitting further diminishes after the band crossing.

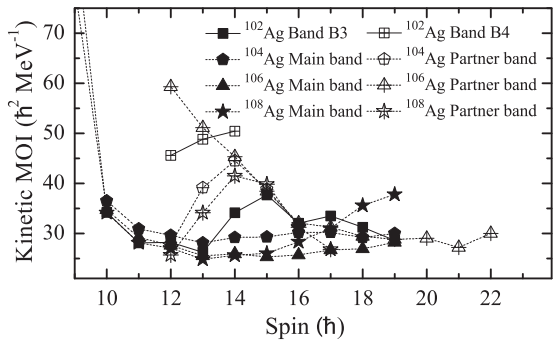

FIG. 8. The kinetic moment of inertia comparison of doublet bands in doubly odd $^{102-108}$Ag [13,15,16,18,20].

Band B4 decays from its various states to the states in band B3 and the decay pattern is similar to that expected for the chiral partner candidate. Also, the excitation energy vs spin plot for band B4 lies close and above band B3 [Fig. 5(a)]. The Routhian (e') plots and excitation energy vs spin plots for the degenerate negative-parity bands in the ^{104,106,108}Ag isotopes [13,15,16,18,20] similar to bands B3 and B4 in ^{102}Ag are included in Figs. 6(b)–6(d) and Figs. 5(b)–5(d), respectively. The $\pi g_{9/2} \otimes \nu h_{11/2}$ band is labeled as main band and the excited negative-parity band is labeled as partner band. In ^{106,108}Ag [15,16,18,20], crossing between two similar structures is observed at $I = 14\hbar$ and $16\hbar$, respectively. In ^{104}Ag, the crossing of doublet bands is not observed even up to $I \sim 16\hbar$. The Routhian (e') plots exhibit increasing energy difference, 0.94, 1.22, 1.48, and 1.70 MeV with increasing neutron number in the doubly odd ^{102,104,106,108}Ag isotopes. The kinetic moment of inertia (MOI) values have been plotted for the nearly degenerate bands in the doubly odd ^{102,104,106,108}Ag isotopes [13,15,16,18,20] (Fig. 8). Band B3 in ^{102}Ag shows much lower values of MOI compared with that of band B4. Similar trends are observed in the heavier ^{104,106,108}Ag isotopes. Also, the experimentally determined B($M1$) $\sim 1.0\ \mu_N^2$ and B($E2$) $\sim 0.05 e^2\mathrm{b}^2$ values for band B4 also differ significantly from the respective values $\sim 0.3\mu_N^2$ and $\sim 0.02\ e^2\mathrm{b}^2$ for band B3 [Figs. 9(a) and 9(d)]. The observed differences infer bands B3 and B4 are not likely to be chiral partners and have different underlying structures. Band B4 in ^{102}Ag exhibits high alignment and a small signature splitting of ∼40 keV. It can be a four-quasiparticle band with $\pi g_{9/2} \otimes \nu h_{11/2}(d_{5/2}/g_{7/2})^2$ and $\pi g_{9/2} \otimes \nu h_{11/2}{}^3$ as likely candidates. However, the latter configuration is unlikely on the basis of additivity of alignment arguments.

To gain further insight into the deformation and electromagnetic properties of doublet bands B3 and B4 in ^{102}Ag, the experimental results are compared with those obtained from the hybrid version of the TAC model calculations [22,23]. The TAC approach has been used extensively to study the deformed density distribution and excited structural features in nearly spherical nuclei and have successfully explained the experimentally observed features related to triaxiality in nuclei in the $A \sim 100$ mass region [43]. Various expected configurations, viz., $\pi g_{9/2} \otimes \nu h_{11/2}$, $\pi g_{9/2} \otimes \nu h_{11/2}(d_{5/2}/g_{7/2})^2$, and $\pi g_{9/2} \otimes \nu h_{11/2}^3$ inferred from the systematic in the mass

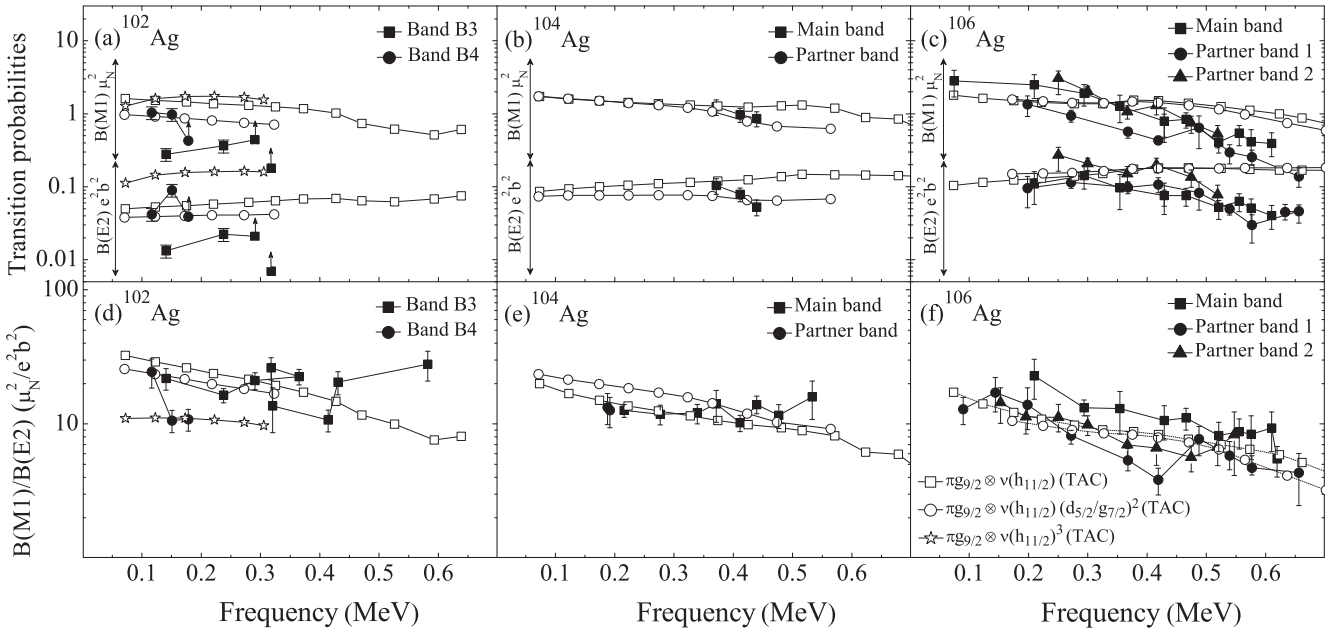

FIG. 9. The comparison of the experimental and theoretical reduced transition probabilities, B($M1$) and B($E2$), for the main band and the partner band in the (a) ^{102}Ag, (b) ^{104}Ag [13], and (c) ^{106}Ag [15,16,20] isotopes. The comparison of the experimental and theoretical B($M1$)/B($E2$) values for the main band and the partner band in the (d) ^{102}Ag, (e) ^{104}Ag [13], and (f) ^{106}Ag [15,16,20] isotopes.

$A \sim 100$ region, are considered for the TAC model calculations for the negative-parity bands in the ^{102}Ag nucleus. In these calculations, the pairing parameters are chosen as 80% of the odd-even mass difference, i.e., $\Delta\pi = 0.925$ MeV and $\Delta\nu = 0.786$ MeV. The quadrupole deformation parameter ϵ_2, the hexadecapole deformation parameter ϵ_4, the triaxiality parameter γ, and the average tilt angle θ calculated for various configurations in ^{102}Ag are given in Table III. The plots for the experimental and theoretical B($M1$) and B($E2$) values, and their ratios vs frequency are given in Figs. 9(a) and 9(d), respectively, and that for the spin vs frequency are given in Fig. 10(a).

The TAC calculations predict that band based on the $\pi g_{9/2} \otimes \nu h_{11/2}^3$ configuration occurs at higher excitation energy [Fig. 5(a)], which is beyond the regime observable in the present experiment. This configuration is unlikely for bands B3 and B4. Remarkable agreement between the experimental and theoretical (i) excitation energy vs spin plot [Fig. 5(a)] and (ii) spin vs frequency plot [Fig. 10(a)] prompt for assignment of the $\pi g_{9/2} \otimes \nu h_{11/2}$ configuration for band B3. The $\pi g_{9/2} \otimes \nu h_{11/2}(d_{5/2}/g_{7/2})^2$ configuration well reproduces the experimental excitation [Fig. 5(a)] and spin vs frequency plots of band B4 [Fig. 10(a)]. It is interesting to note that the $\pi g_{9/2} \otimes \nu h_{11/2}$ band (band B3) coexists even in the presence of band B4 based on the $\pi g_{9/2} \otimes \nu h_{11/2}(d_{5/2}/g_{7/2})^2$ configuration involving an aligned pair. The diabatical crossing of bands B3 and B4 at $I \sim 14\hbar$ is also well supported by theoretical calculations. Note that no other minima has been observed in the $\pi g_{9/2} \otimes \nu h_{11/2}$ configuration until the frequency ~0.4 MeV. Therefore, shape transition is unlikely. It is worth mentioning that the TAC model calculations for the $\pi g_{9/2} \otimes \nu h_{11/2}(d_{5/2}/g_{7/2})^2$ configuration do not permit a continuation of the band beyond $I \sim 14\hbar$ due to large gap in the Nilsson orbitals. The B($M1$)/B($E2$) values observed for bands B3 and B4 are large ~10–28 $\mu_N^2\ e^{-2}\mathrm{b}^{-2}$, which exhibit good agreement with the TAC calculations for the assigned configurations [Fig. 9(a)]. The calculated B($M1$) and B($E2$) values exhibit conformity with the experimental ones in the case of band B4 [Fig. 9(d)]; however, the calculated results are higher by factor of two to five for band B3.

TABLE III. TAC model parameters calculated for the various configurations in $^{102-108}$Ag.

Isotope	Configuration	ϵ_2	ϵ_4	γ	θ
	$\pi g_{9/2} \otimes \nu h_{11/2}$	0.132	−0.019	12.5°	68°
^{102}Ag	$\pi g_{9/2} \otimes \nu h_{11/2}(d_{5/2}/g_{7/2})^2$	0.121	−0.016	14.9°	65°
	$\pi g_{9/2} \otimes \nu_{11/2}^3$	0.155	−0.030	−6.4°	61°
^{104}Ag	$\pi g_{9/2} \otimes \nu h_{11/2}$	0.158	−0.006	6.5°	74°
	$\pi g_{9/2} \otimes \nu h_{11/2}(d_{5/2}/g_{7/2})^2$	0.144	−0.004	13.1°	69°
^{106}Ag	$\pi g_{9/2} \otimes \nu h_{11/2}$	0.172	0.004	4.8°	74°
	$\pi g_{9/2} \otimes \nu h_{11/2}(d_{5/2}/g_{7/2})^2$	0.168	0.004	0°	78°
^{108}Ag	$\pi g_{9/2} \otimes \nu h_{11/2}$	0.185	0.009	0°	73°
	$\pi g_{9/2} \otimes \nu h_{11/2}(d_{5/2}/g_{7/2})^2$	0.138	0.001	0°	66°

To obtain a systematic view of properties of the degenerate bands, the TAC model calculations for the $\pi g_{9/2} \otimes \nu_{11/2}$ and $\pi g_{9/2} \otimes \nu h_{11/2}(d_{5/2}/g_{7/2})^2$ configurations are also performed for the neighboring heavier doubly odd ^{104,106,108}Ag isotopes. The deformation parameters ϵ_2, ϵ_4, γ, and θ parameters used in calculations for various configurations are listed in Table III. The experimental and TAC calculated excitation energy vs spin and spin vs frequency are plotted for the ^{102,104,106,108}Ag isotopes in Figs. 5 and 10, respectively. The plots exhibit good agreement. The observed diabatic crossing

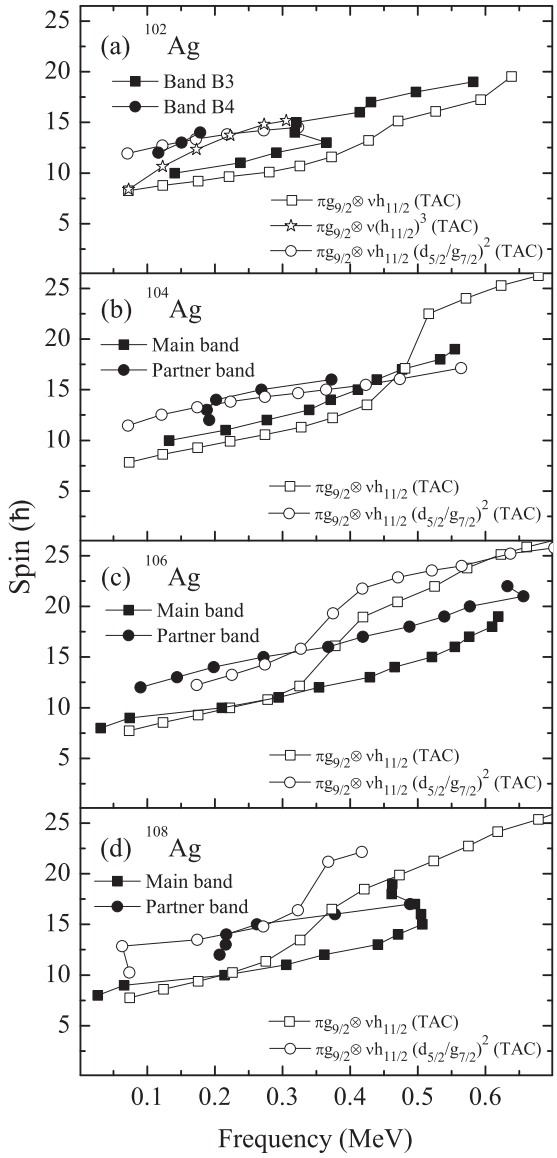

FIG. 10. The spin I vs frequency $\hbar\omega$ plots for the observed negative-parity doublet bands in (a) ^{102}Ag, (b) ^{104}Ag [13], (c) ^{106}Ag [15,16,20], and (d) ^{108}Ag [18] isotopes. The results of the TAC calculations based on different relevant configurations are also shown for comparison.

in ^{104}Ag is well reproduced in the TAC calculations wherein for ^{106,108}Ag, the predicted crossing occurs at higher frequency. The TAC-calculated B(M1) and B(E2) values and their ratios for the ^{104,106}Ag isotopes are compared with the measured values [13,20] in Fig. 9 and reasonably good agreement is observed. Leider *et al.* [20] have also concluded that the partner band in ^{106}Ag results from a four-quasiparticle $\pi g_{9/2} \otimes \nu h_{11/2}(d_{5/2}/g_{7/2})^2$ configuration on the basis of adiabatic and configuration-fixed constrained triaxial relativistic-mean-field calculations and particle-rotor model (PRM) calculations. The TAC-calculated B(M1)/B(E2) values in ^{108}Ag are also in good agreement with the available experimental results [18]. The measured B(M1) and B(E2) values in ^{108}Ag are not available in the literature.

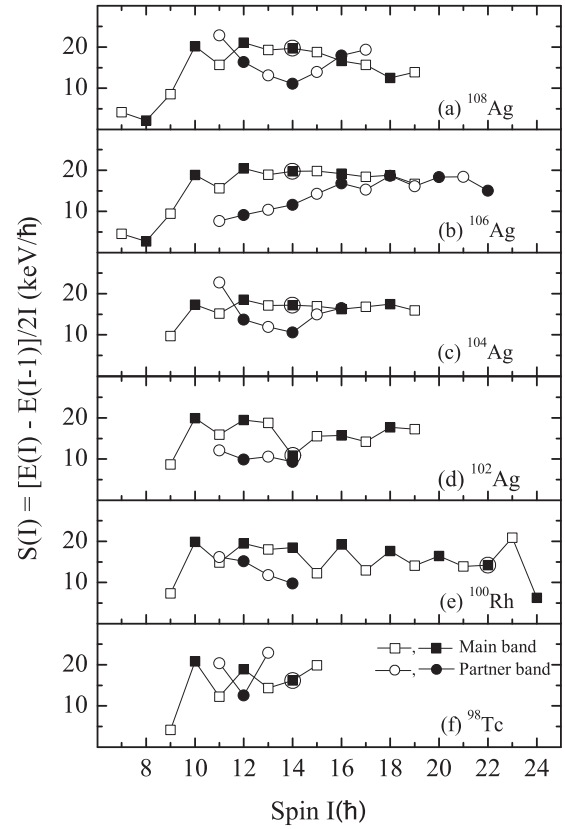

FIG. 11. Plot of energy-staggering parameter $S(I) = [E(I) - E(I-1)]/2I$ for (a)–(d) the doubly odd $^{102-108}$Ag isotopes [13,15,16,18,20], and (e), (f) $N = 55$ isotones ^{98}Tc [7] and ^{100}Rh [9] plotted as a function of spin $I(\hbar)$. The signature inversion spin values are encircled.

To have a glimpse of the signature splitting systematics for the $\pi g_{9/2} \otimes \nu h_{11/2}$ and excited negative-parity bands in the doubly odd $^{102-108}$Ag isotopes and the neighboring doubly odd isotones ^{100}Rh and ^{98}Tc of ^{102}Ag, the staggering parameter $S(I) = [E(I) - E(I-1)]/2I$ is plotted in Fig. 11. The $\pi g_{9/2} \otimes \nu h_{11/2}$ bands exhibit anomalous signature splitting in these nuclei above the $J_n + j_p = 10\hbar$. Signature inversion is observed at $\sim 14\hbar$ in the ^{102,104,106,108}Ag isotopes. The theoretical calculations predict small γ values for these $\pi g_{9/2} \otimes \nu h_{11/2}$ bands (Table III), which is not sufficient to explain the observed signature inversion in this mass region. The competition between coriolis and proton-neutron interaction [44] can cause for the signature inversion. The excited negative-parity band in ^{98}Tc [Fig. 11(f)] and ^{102}Ag show signature splitting out of phase with that of the $\pi g_{9/2} \otimes \nu h_{11/2}$ band [Fig. 11(d)] whereas the two bands are in phase in the case of ^{100}Rh [Fig. 11(e)].

V. CONCLUSION

The level scheme of the doubly odd ^{102}Ag nucleus has been studied by using in-beam γ-ray spectroscopic techniques following its population in the ^{75}As(^{31}P, $p3n$) fusion evaporation reaction at $E_{\rm lab} = 125$ MeV. The previous level scheme of the doubly odd ^{102}Ag nucleus is substantially modified and extended up to spin $19\hbar$. A new excited negative-parity dipole

band has been identified and decays through $\Delta I = 0$, 1, and 2 transitions from its various states to respective states in the negative-parity dipole $\pi g_{9/2} \otimes \nu h_{11/2}$ band as well as the positive-parity $\pi g_{9/2} \otimes \nu d_{5/2}$ and $\pi g_{9/2} \otimes \nu g_{7/2}$ bands. The B($M1$) and B($E2$) values are deduced for the negative-parity dipole bands from the present DSAM measurements. Difference in kinetic moment of inertia, B($M1$) and B($E2$) transition probabilities for these negative-parity, nearly degenerate bands do not favor these bands to be chiral partners. The TAC model calculations well reproduce the observed deformation and electromagnetic properties of the nearly degenerate pair of bands with the assigned $\pi g_{9/2} \otimes \nu h_{11/2}$ and $\pi g_{9/2} \otimes \nu h_{11/2}(d_{5/2}/g_{7/2})^2$ configurations. These observations and interpretation are systematically consistent for the nearly degenerate bands observed in the doubly odd $^{102-108}$Ag isotopes.

ACKNOWLEDGMENTS

We would like to thank the TIFR-BARC Pelletron Linac Facility staff for providing a good-quality beam. The help and cooperation of the members of the INGA collaboration for setting up the array are acknowledged. The authors would also like to thank the Department of Science and Technology, Government of India, for providing funding for the INGA project (No. IR/S2/PF-03/2003-I). Financial support from IUAC, New Delhi for Project No. IUAC/XIII.7/UFR-50302, UGC, New Delhi for Project No. 42-809/2013 (SR), and DST FIST are duly acknowledged. Financial support from UGC, New Delhi, under the Centre of Advanced Study Funds and Basic Scientific Research fellowship in Sciences (for V.S.) are duly acknowledged.

[1] R. M. Clark and A. O. Macchiavelli, Annu. Rev. Nucl. Part. Sci. **50**, 1 (2000).
[2] A. J. Simons, R. Wadsworth, D. G. Jenkins, R. M. Clark, M. Cromaz, M. A. Deleplanque, R. M. Diamond, P. Fallon, G. J. Lane, I. Y. Lee, A. O. Macchiavelli, F. S. Stephens, C. E. Svensson, K. Vetter, D. Ward, and S. Frauendorf, Phys. Rev. Lett. **91**, 162501 (2003).
[3] S. Roy *et al.*, Phys. Lett. B **694**, 322 (2011).
[4] W. Reviol *et al.*, Nucl. Phys. A **557**, 391 (1993).
[5] J. Gizon *et al.*, Z. Phys. A: Hadrons Nucl. **345**, 335 (1993).
[6] V. I. Dimitrov, S. Frauendorf, and F. Dönau, Phys. Rev. Lett. **84**, 5732 (2000).
[7] H.-B. Ding *et al.*, Chin. Phys. Lett. **27**, 072501 (2010).
[8] P. Joshi *et al.*, Eur. Phys. J. A **24**, 23 (2005).
[9] A. Gizon *et al.*, Eur. Phys. J. A **2**, 325 (1998).
[10] D. Tonev, M. S. Yavahchova, N. Goutev, G. de Angelis, P. Petkov, R. K. Bhowmik, R. P. Singh, S. Muralithar, N. Madhavan, R. Kumar, M. Kumar Raju, J. Kaur, G. Mohanto, A. Singh, N. Kaur, R. Garg, A. Shukla, T. K. Marinov, and S. Brant, Phys. Rev. Lett. **112**, 052501 (2014).
[11] I. Kuti, Q. B. Chen, J. Timar, D. Sohler, S. Q. Zhang, Z. H. Zhang, P. W. Zhao, J. Meng, K. Starosta, T. Koike, E. S. Paul, D. B. Fossan, and C. Vaman, Phys. Rev. Lett. **113**, 032501 (2014).
[12] J. Meng, J. Peng, S. Q. Zhang, and S.-G. Zhou, Phys. Rev. C **73**, 037303 (2006).
[13] Z. G. Wang, M. L. Liu, Y. H. Zhang, X. H. Zhou, B. T. Hu, N. T. Zhang, S. Guo, B. Ding, Y. D. Fang, J. G. Wang, G. S. Li, Y. H. Qiang, S. C. Li, B. S. Gao, Y. Zheng, W. Hua, X. G. Wu, C. Y. He, Y. Zheng, C. B. Li, J. J. Liu, and S. P. Hu, Phys. Rev. C **88**, 024306 (2013).
[14] J. Timar, T. Koike, N. Pietralla, G. Rainovski, D. Sohler, T. Ahn, G. Berek, A. Costin, K. Dusling, T. C. Li, E. S. Paul, K. Starosta, and C. Vaman, Phys. Rev. C **76**, 024307 (2007).
[15] P. Joshi, M. P. Carpenter, D. B. Fossan, T. Koike, E. S. Paul, G. Rainovski, K. Starosta, C. Vaman, and R. Wadsworth, Phys. Rev. Lett. **98**, 102501 (2007).
[16] N. Rather, P. Datta, S. Chattopadhyay, S. Rajbanshi, A. Goswami, G. H. Bhat, J. A. Sheikh, S. Roy, R. Palit, S. Pal, S. Saha, J. Sethi, S. Biswas, P. Singh, and H. C. Jain, Phys. Rev. Lett. **112**, 202503 (2014).
[17] B. Qi, H. Jia, N. B. Zhang, C. Liu, and S. Y. Wang, Phys. Rev. C **88**, 027302 (2013).
[18] J. Sethi *et al.*, Phys. Lett. B **725**, 85 (2013).
[19] H.-L. Ma, S.-H. Yao, B.-G. Dong, X.-G. Wu, H.-Q. Zhang, and X.-Z. Zhang, Phys. Rev. C **88**, 034322 (2013).
[20] E. O. Lieder, R. M. Lieder, R. A. Bark, Q. B. Chen, S. Q. Zhang, J. Meng, E. A. Lawrie, J. J. Lawrie, S. P. Bvumbi, N. Y. Kheswa, S. S. Ntshangase, T. E. Madiba, P. L. Masiteng, S. M. Mullins, S. Murray, P. Papka, D. G. Roux, O. Shirinda, Z. H. Zhang, P. W. Zhao, Z. P. Li, J. Peng, B. Qi, S. Y. Wang, Z. G. Xiao, and C. Xu, Phys. Rev. Lett. **112**, 202502 (2014).
[21] W. A. Dar, J. A. Sheikh, G. H. Bhat, R. Palit, R. N. Ali, and S. Frauendorf, Nucl. Phys. A **933**, 123 (2015).
[22] V. I. Dimitrov, F. Dönau, and S. Frauendorf, Phys. Rev. C **62**, 024315 (2000).
[23] S. Frauendorf and J. Meng, Nucl. Phys. A **617**, 131 (1997).
[24] S. Muralithar *et al.*, Nucl. Instrum. Methods Phys. Res., Sect. A **622**, 281 (2010).
[25] R. Palit *et al.*, Nucl. Instrum. Methods Phys. Res., Sect. A **680**, 90 (2012).
[26] D. C. Radford, Nucl. Instr. Meth. A **361**, 297 (1995); **361**, 306 (1995).
[27] S. Kumar *et al.*, J. Phys. G **41**, 105110 (2014).
[28] A. Krämer-Flecken, T. Morek, R. M. Lieder, W. Gast, G. Hebbinghaus, H. M. Jäger, and W. Urban, Nucl. Instrum. Methods Phys. Res., Sect. A **275**, 333 (1989).
[29] J. Timar, J. Gizon, A. Gizon, D. Sohler, B. M. Nyako, L. Zolnai, A. J. Boston, D. T. Joss, E. S. Paul, A. T. Semple, C. M. Parry, and I. Ragnarsson, Phys. Rev. C **62**, 044317 (2000).
[30] K. Starosta *et al.*, Nucl. Instrum. Methods Phys. Res., Sect. A **423**, 16 (1999).
[31] J. C. Wells, ORNL Physics Division, Progress Report No. ORNL-6689 (1991), p. 44.
[32] L. C. Northcliffe and R. F. Schilling, At. Data Nucl. Data Tables **7**, 233 (1970).
[33] F. James and M. Roos, Comput. Phys. Commun. **10**, 343 (1975).
[34] D. De Frenne, Nucl. Data Sheets **110**, 1745 (2009).
[35] S. Rastikerdar, Phys. At. Nucl. **64**, 1210 (2001).
[36] V. Ravi Kumar *et al.*, Z. Phys. A: Hadrons Nucl. **351**, 249 (1995).
[37] J. Tréherne *et al.*, Phys. Rev. C **27**, 166 (1983).
[38] D. Sohler *et al.*, Nucl. Phys. A **733**, 37 (2004).
[39] H. B. Zhou *et al.*, Eur. Phys. J. A **47**, 107 (2011).

[40] V. Singh, S. Sihotra, J. Goswamy, N. Singh, S. Saha, J. Sethi, R. Palit, Z. Naik, and D. Mehta, Proc. DAE-BRNS Symp. Nucl. Phys. **60**, 180 (2015); **59**, 224 (2014).

[41] S. Ray, N. S. Pattabiraman, Krishichayan, A. Chakraborty, S. Mukhopadhyay, S. S. Ghugre, S. N. Chintalapudi, A. K. Sinha, U. Garg, S. Zhu, B. Kharraja, and D. Almehed, Phys. Rev. C **77**, 024305 (2008).

[42] R. Bengtsson and S. Frauendorf, Nucl. Phys. A **327**, 139 (1979).

[43] S. Kumar, S. Sihotra, K. Singh, V. Singh, Sandeep, J. Goswamy, N. Singh, D. Mehta, S. S. Malik, R. Palit, R. Kumar, R. P. Singh, S. Muralithar, and R. K. Bhowmik, Phys. Rev. C **89**, 034303 (2014).

[44] J. Timár *et al.*, Acta Phys. Pol. B **33**, 493 (2002).